Magnetism and structural distortions in uranium sulfide under pressure

J. R. Jeffries,[1] P. Söderlind,[1] H. Cynn,[1] A. Landa,[1] W. J. Evans,[1] S. T. Weir,[1] Y. K. Vohra,[2] and G. H. Lander[3]

[1]*Condensed Matter and Materials Division, Lawrence Livermore National Laboratory, Livermore, California 94550, USA*
[2]*Department of Physics, University of Alabama at Birmingham, Birmingham, Alabama 35924, USA*
[3]*European Commission, Joint Research Centre, Institute for Transuranium Elements, Postfach 2340, D-76125 Karlsruhe, Germany*

Uranium sulfide belongs to a class of uranium monochalcogenides that crystallize in the rocksalt structure and exhibit ferromagnetism at low temperature. The magnetism is believed to play a role in the low-temperature rhombohedral distortion, possibly due to its large magnetic anisotropy. We have performed electrical and structural characterization along with density-functional theory calculations as functions of pressure to help understand the interplay between structure and magnetism in US. Theoretical calculations suggest that ferromagnetic order is responsible for the small distortion at ambient pressure and low temperature. Under pressure, the Curie temperature is reduced monotonically until it discontinuously disappears near a pressure-induced deformation of the crystal structure. This high-pressure distortion is identical to the one correlated with the onset of magnetic order, but with a larger change in the cell angle. Calculations imply a reduction in the electronic band energy as the driving force for the pressure-induced structure, but the loss of magnetic order associated with this distortion remains a mystery. The high-pressure electronic phase diagram may shed light on the magnetostructural free energy landscape of US.

PACS number(s): 64.60.Ej, 75.50.Cc

I. INTRODUCTION

Uranium sulfide is a member of the ferromagnetic uranium monochalcogenides UX (i.e., US, USe, and UTe), which, under ambient conditions, crystallize in a simple rocksalt (B1-$Fm\bar{3}m$) structure. The uranium monochalcogenides have been widely studied owing to their simple crystal structure and the ability to tune lattice volumes and electronic structure based on the chalcogen size.[1] US is paramagnetic at room temperature with a moment of 2.2 μ_B, lower than the expectations of a localized f^2 or f^3 configuration for the U ions.[2] Below 177 K, US undergoes concomitant magnetic and structural transitions, resulting in a ferromagnetic ground state and a rhombohedral unit cell.[2–6] This rhombohedral unit cell is best described as a small distortion of the cubic rocksalt structure along one of the [111] directions. The ferromagnetic state is characterized by an ordered moment of about 1.55 μ_B, manifesting from the sum of a U ion contribution of 1.7 μ_B and an antiparallel contribution from the spd conduction electrons of -0.15 μ_B.[2,7] The magnetic easy axis is directed along the body diagonal [111] direction of the former rocksalt structure, resulting in one of the largest magnetic anisotropies in a cubic system.[4] No qualitative explanation to this structural phase transition has heretofore been put forward, although there are speculations that the rhombohedral distortion is a consequence of the magnetostriction arising from the ferromagnet order.[5,6]

The magnetism in US originates from the 5f electrons in uranium that produce both spin and orbital moments. The 5f spin moment is somewhat smaller (1.30 μ_B) than the antiparallel orbital moment (-3.0 μ_B)[8–10] as is expected from the fact that the 5f band is less than half filled with a substantial spin-orbit interaction.[11] Both the paramagnetic and ferromagnetic states of US, however, exhibit moments below the expectations of purely localized f states, suggesting a strong itinerant component to the f states. This itinerancy is corroborated by specific heat measurements that imply an enhanced γ as well as photoemission spectra that reveal

a strong 5f peak near the Fermi level.[12–15] Additionally, measurements of the lattice dynamics of US suggest that f-d hybridization[16] is responsible for the small Poisson's ratio as well as a small U-U interatomic force constant, which leads to an anomalously small bulk modulus with respect to the lattice volume.[17] These measurements point to the importance of the electronic structure, particularly the behavior of the U 5f states, in determining the physical properties of this crystallographically simple material.

Under pressure at room temperature, US distorts from its ambient-pressure B1 phase to a rhombohedral phase near 10 GPa.[18] For pressures above 30 GPa, hints of another transformation in US may be evident, although peak broadening and questions of strain from the pressure medium prevented Gerward and coworkers from concluding a phase transition.[18] This pressure-induced rhombohedral distortion in US contrasts with the behavior of USe and UTe, for which pressure induces a B1-B2 transition (CsCl type, $Pm\bar{3}m$).[18] For USe and UTe, the transition to the B2 phase causes an abrupt destruction of ferromagnetic ordering.[20]

The rhombohedral phase of US seen above 10 GPa is identical to the low-temperature distortion seen upon entering the ferromagnetic state; however, the ferromagnetic state is not enhanced with pressure. Instead, as shown by ac susceptibility measurements in a diamond anvil cell, the Curie temperature T_C of US is suppressed monotonically up to approximately 10 GPa, abruptly disappearing, just as the ferromagnetic states of USe and UTe, for pressures in excess of 10 GPa.[19,20] The behavior of T_C under pressure for the UX system has been described theoretically by a competition between increasing hybridization strength and decreasing f occupancy.[21] The spin and orbital moments of US have been shown theoretically to vary by only a small amount with increasing pressure,[22] precluding a quenching of U moments as a mechanism for the destruction of magnetic order. The destruction of magnetic order in USe and UTe is associated with first-order

phase transitions and concomitant discontinuous reductions in atomic volume, suggesting that magnetic order is tied to the symmetry of the crystal structure. The case for US is a bit different, however, as the structural phase transition associated with the loss of magnetic order seems to be continuous with no volume discontinuity. The loss of magnetic order in US is thus puzzling, either indicating its deviation from the other members of the UX system or implying other, unknown mechanisms shared within the UX system. In the present study we apply experimental methods to investigate structural and electrical transport properties combined with electronic-structure calculations at elevated pressures to help shed light on these interesting behaviors of US.

II. EXPERIMENTAL AND THEORETICAL METHODS

A. Electrical transport

Single crystals of US were previously grown by a recrystallization process.[23] High-pressure electrical transport measurements were performed as a function of temperature and magnetic field using a nonmagnetic designer diamond anvil cell (DAC) in combination with a commercial low-temperature cryostat equipped with a 16-T superconducting magnet (Quantum Design PPMS). The DAC consisted of a conventional diamond anvil paired with an 8-probe designer diamond anvil;[24–26] both anvils had 300-μm culets. The tungsten microprobes of the designer diamond were lithographically capped with tungsten contact pads to facilitate electrical contact. An MP35N gasket was pre-indented down to a thickness of 40 μm, and a hole, to serve as the high-pressure sample chamber, was drilled in the center of the indentation using an electric discharge machine (EDM). The sample chamber was packed with solid steatite, which served as the pressure-transmitting medium, and several ruby chips, which were used as pressure calibrants.[27,28] The single-crystal sample was cut with a razor blade and placed in contact with the electrical contact pads on the designer anvil. Electrical resistivity measurements were performed with the standard, four-probe technique. The lead geometry was established by the pattern of the designer anvil, which lent itself easily to a transverse and longitudinal transport geometry.

B. Structural characterization

X-ray diffraction measurements were performed in a membrane-driven DAC comprising 300-μm-culet diamond anvils. A rhenium gasket was pre-indented down to 40 μm, and a 120-μm hole was drilled with an EDM. Powdered uranium sulfide was loaded into the sample chamber along with a small amount of copper powder, the measured lattice compression of which provided a pressure marker. The DAC was sealed under a high-pressure of neon, which served as the pressure-transmitting medium. Angle-dispersive x-ray diffraction measurements were performed at the HPCAT beamline 16 BM-D of the Advanced Photon Source at Argonne National Laboratory using a 5 × 10 μm microfocused beam. Two incident wavelengths were used ($\lambda = 0.3676$ Å and $\lambda = 0.4246$ Å) for different experiments at room temperature and low temperatures. Low-temperature data were collected using a helium-flow cryostat to control temperature; standard

Si diodes were used to measure the temperature. Diffraction data were collected on a Mar345 image plate using 30–120 second acquisitions. Two-dimensional diffraction patterns were integrated with FIT2D,[29] and structural refinements were performed with the JADE software package.

C. Theoretical modeling

The electronic-structure modeling is here framed within the density-functional theory (DFT) with the necessary assumption for the electron exchange and correlation functional chosen to be the generalized-gradient approximation (GGA)[34] as currently being the best starting point for actinide DFT calculations.[30,31] Most calculations are performed utilizing an all-electron full-potential linear muffin-tin orbitals (FPLMTO) approach that has been described in detail.[35] This FPLMTO implementation has been used extensively and successfully for transition[32] and actinide[33] metals. The "full potential" refers to the use of nonspherical contributions to the electron charge density and potential. This is accomplished by expanding these in cubic harmonics inside nonoverlapping muffin-tin spheres and in a Fourier series in the interstitial region. We use two energy tails associated with each basis orbital and for the semicore $6s$, $6p$, and valence $7s$, $7p$, $6d$, and $5f$ states, these pairs are different. Spherical harmonic expansions are carried out through $l_{max} = 8$ for the bases, potential, and charge density. Because we are studying an actinide system, one has to consider the possibility that electron correlations such as the spin-orbit interaction and orbital polarization may be important. However, strong electron correlations leading to $5f$-orbital localization is not considered because US is believed to possess itinerant (band-like) $5f$ states.[36] The technical details of the FPLMTO calculations are very similar to those performed earlier for plutonium metal.[37–39] Here different magnetic order (ferromagnetic and antiferromagnetic) and even magnetic disorder combined with spin-orbit coupling and orbital polarization are applied.

Spin-orbit coupling is implemented in a first-order variational procedure[40] for the valence d and f states, as was done previously,[41] and for the core states the fully relativistic Dirac equation is solved. The inclusion of spin-orbit coupling for the $5f$ states of uranium may be essential, since it has been experimentally shown to be strong in actinide metals.[42] The orbital polarization was shown to be significant in plutonium metal[43] and is here included as described by Eriksson *et al.*[44] The energy of the orbitals with the spin, orbital, and magnetic quantum numbers (σ, l, m_l) is shifted an amount proportional to $L_\sigma m_l$. Here L_σ is the total orbital moment from electrons with spin σ. This self-consistent parameter-free technique attempts to generalize Hund's second rule for an atom to a bulk condensed-matter state, and enhances the separation of the m_l orbitals caused by the spin-orbit interaction. Hence, the orbital polarization can be viewed as an amplification of the spin-orbit coupling. The orbital polarization mechanism is also known to improve on the calculated orbital magnetic moments in US.[45] Both the [111] and [100] directions of the spin moment are considered both in the ferromagnetic and antiferromagnetic order.

The phases we are investigating for US all have relatively small unit cells. The B1 and B2 phases are cubic with two

atoms per unit cell, while the *Immm* phase is a 4-atom orthorhombic phase ($b/a = 1.036$ and $c/a = 1.435$), which is a small distortion of a higher symmetry phase ($c/a = 1.0$ and $c/a = \sqrt{2}$), where the uranium atoms occupy the face-centered-cubic lattice positions. The *Immm* phase was simulated, because it was found to be a candidate structure, albeit a weaker one, based on x-ray diffraction experiments. The axial ratios of the *Immm* phase are allowed to relax during the compression. A rhombohedral strain on the B1 phase changes the cubic angle α to something different than 90 degrees and results in the $R\bar{3}m$ phase. A large number of *k* points are chosen and close to about 1000 for all phases in the full Brillouin zone.

For the disordered magnetic calculations we are using the disordered-local-moment (DLM) approach. For this purpose we apply the so-called exact muffin-tin orbitals (EMTO) method[46] that includes spin-orbit effects.[47] Here the one-electron potential is represented by optimized overlapping muffin-tin (OOMT) potential spheres, where inside the potential spheres the potential is spherically symmetric, whereas it is constant between the spheres. The radii of the potential spheres, the spherical potentials inside the spheres, and the constant value in the interstitial region are determined by minimizing (i) the deviation between the exact and overlapping potentials, and (ii) the errors caused by the overlap between the spheres. Within the EMTO formalism, the one-electron states are calculated exactly for the OOMT potentials. As an output of the EMTO calculations, one can determine the self-consistent Green's function of the system and the complete, non-spherically symmetric charge density. Finally, the total energy is calculated using the full charge-density technique.[48]

The calculations are performed for a basis set including valence *spdf* orbitals. For the electron exchange and correlation energy functional, the GGA is considered.[34] Magnetism is modeled within the DLM approximation; i.e., the uranium metal is viewed as an alloy $U1_{50}U2_{50}$ with U1 and U2 having opposite spin direction. The alloy treatment in EMTO is performed within the coherent potential approximation and the DLM solution is equivalent to a paramagnetic state; see Ref. [49] for details.

III. RESULTS

A. Electronic structure calculations

Uranium compounds can have varying degrees of localization of the uranium 5*f* electrons. In the case of US it has been proposed that the 5*f* states can accurately be modeled by band (itinerant) states in DFT,[36] because of the existence of a sharp peak of the photoemission close to the Fermi level. A simple, albeit indirect, analysis of the 5*f* bonding strength is to calculate the equilibrium volume, assuming itinerant or localized 5*f* electrons, and compare with experiment. In Table I we list the results from calculations assuming itinerant and localized (standard rare-earth model with the *f* electrons in the core) 5*f* states with experimental room-temperature data. The itinerant 5*f* model agrees quite well with the measured data in contrast to the localized 5*f* approach, thus suggesting the band picture of the *f* electrons in US.

TABLE I. Theoretical equilibrium volume (V_0) and bulk modulus (B_0) modeled with itinerant (5*f* band) and localized (5*f* localized) uranium 5*f* states together with the room-temperature data discussed in Sec. III B.

Method	V_0 (Å³)	B_0 (GPa)
5*f* band	21.5	105
5*f* localized	24.9	83
Experimental	20.6	106.4

As regards US magnetic properties, our model reproduces the easy axis along the [111] direction with a magnetic anisotropy energy of 31 meV, which is larger than the 14 meV obtained in earlier calculations that do not consider orbital polarization.[50] Our calculated magnetic moments are 2.2 μ_B and $-3.3\ \mu_B$ for the spin and orbital components, respectively. Our model thus overestimates the spin moment (1.3 μ_B) while comparing nicely with the neutron-scattering data for the orbital moment ($-3.0\mu_B$).[2] The aforementioned results are obtained for US in its ambient condition (i.e., the B1 phase), while at temperatures below T_C at about 170 K a rhombohedral distortion is accompanied by ferromagnetic order. It is reasonable to assume that the ferromagnetic order induces the structural distortion through magnetocrystalline effects. To investigate this we calculate the total energy as a function of distortion (cell angle) for three magnetic states, ferromagnetic, nonmagnetic, and paramagnetic (disordered). As shown in Fig. 1, we find that none of these states stabilize the B1 phase (90 degree cell angle) and that the ferromagnetic state is accompanied by a shift in the cell angle. Therefore, we are unable to directly confirm that magnetocrystalline effects stabilize B1. It is plausible, however, that the metastable paramagnetic state in Fig. 1 (D), which is calculated at zero
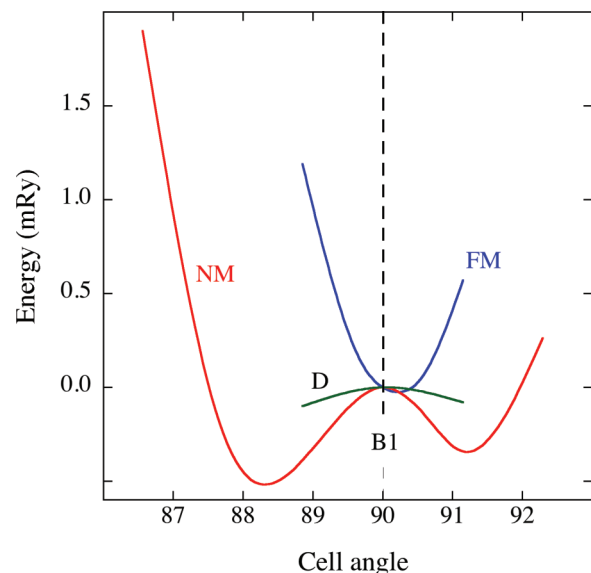

FIG. 1. (Color online) Calculated total energy as a function of cell angle with 90° representing the B1 phase. FM, NM, and D denote the ferromagnetic, nonmagnetic, and disordered magnetic (paramagnetic) configurations, respectively.
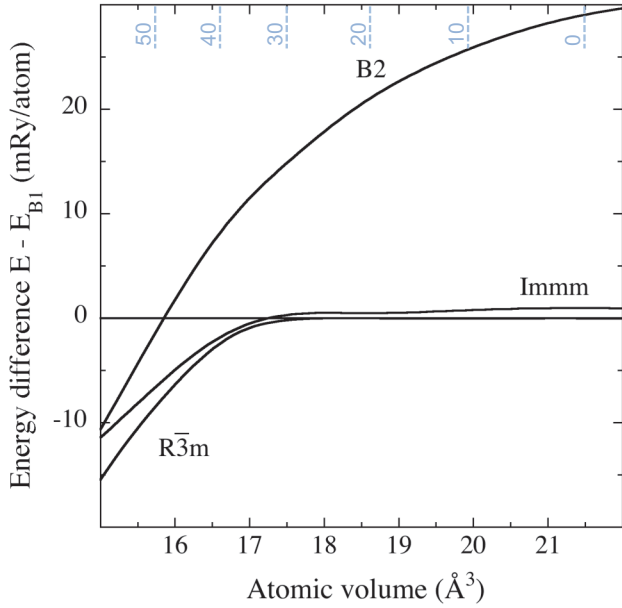
FIG. 2. (Color online) Calculated energy versus atomic volume relative to the B1 phase for the *Immm*, $R\bar{3}m$, and B2 phases, respectively. The calculated pressures corresponding to the atomic volumes of the $R\bar{3}m$ phase are given across the top x axis in GPa.

temperature, could be correct and that thermal entropy is responsible for sustaining the B1 phase above 170 K.

Next, we focus on the behavior of US under compression and compute the total energy of the B1, B2, $R\bar{3}m$ (rhomboderal distortion of B1), and the *Immm* phase. In Fig. 2 we show the total-energy difference for these structures relative to the B1 phase. Notice that the $R\bar{3}m$ phase is predicted to be stable for all volumes down to 15 Å^3 (62 GPa). The rhombohedral distortion drives the cell angle away from the higher symmetry 90° angle, producing an $R\bar{3}m$ cell with either a larger or smaller cell angle. These angles are roughly symmetric about 90°, but the DFT model predicts that the larger angle has the lowest energy. However, the energy difference between these two cell angles is small and close to the resolution of the energy calculation. The rhombohedral distortion is predicted to increase with compression and Fig. 3 shows that it becomes
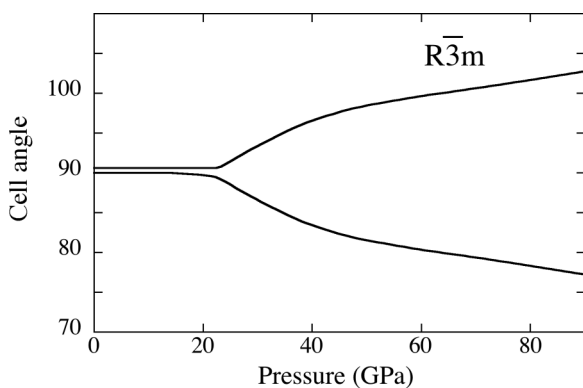

FIG. 3. Calculated rhombohedral distortions (cell angles) of the $R\bar{3}m$ cell as a function of pressure. The larger cell angle is slightly favored in DFT calculations (see text). The 90° angle defines the B1 phase.
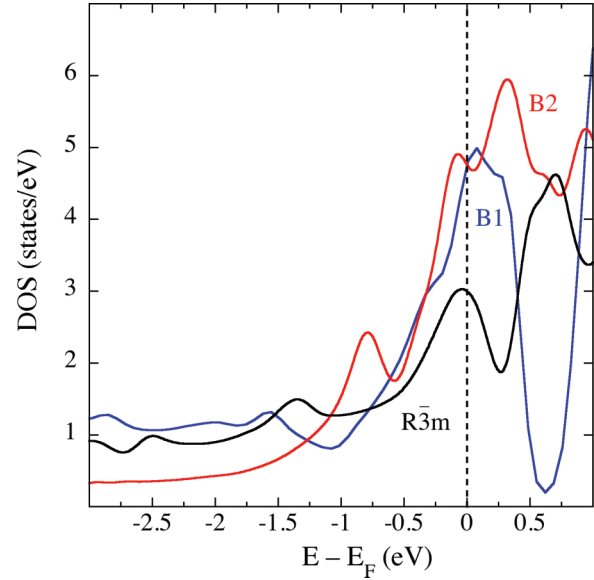

FIG. 4. (Color online) Electronic density of states (DOS) for B1, B2, and the $R\bar{3}m$ phases at about 90 GPa. The dashed vertical line denotes the Fermi level. The $R\bar{3}m$ phase has fewer states occupying higher energies close and below E_F.

a substantial distortion with higher compression. The reason $R\bar{3}m$ is stable over B1 and B2 is found in the electronic density of states (DOS), displayed in Fig. 4. Below the Fermi level (E_F), B1 and B2 have fairly similar DOS, whereas $R\bar{3}m$ has much lower occupied energy states resulting in a lower band energy at about 90 GPa. At this pressure B2 is actually much closer to $R\bar{3}m$ than B1 is (see Fig. 2). The reason for this is that even though the band energy looks to be similar (Fig. 4) between B1 and B2, the latter has a much lower electrostatic energy due to a closer packing of the atoms. This fact will become increasingly important at higher compressions and it is not surprising that the B2 phase has been reported at 80 GPa.[51] In our calculations, however, $R\bar{3}m$ remains stable up to about 100 GPa.

In Fig. 5(a) we show the total (spin and orbital) magnetic moment as a function of atomic volume for the five studied phases. Notice that the moments in B1 and $R\bar{3}m$ are close until complete suppression at about 14.7 Å^3 (~65 GPa). Interestingly, both the B2 and the *Immm* show significantly different magnetic behavior with compression compared to B1 and $R\bar{3}m$. In Fig. 5(b) we display the antiparallel spin and magnetic moments in the $R\bar{3}m$ phase.

B. Crystal structure

Angle-dispersive x-ray diffraction results for US are shown in Fig. 6. At 300 K, and near 1 GPa, the diffraction pattern can be indexed using the B1 structure. The B1 phase remains an excellent description of the data until about 8 GPa. Above 8 GPa, the patterns show preferential peak broadening [e.g., the B1 phase (111) and (220) peaks broaden more with pressure than the (200)]. Above 11 GPa, the peak broadening is sufficient to reduce the quality of the refinements. Consistent with previous experiments and the theoretical calculations above, the data are better fitted using a rhombohedral phase
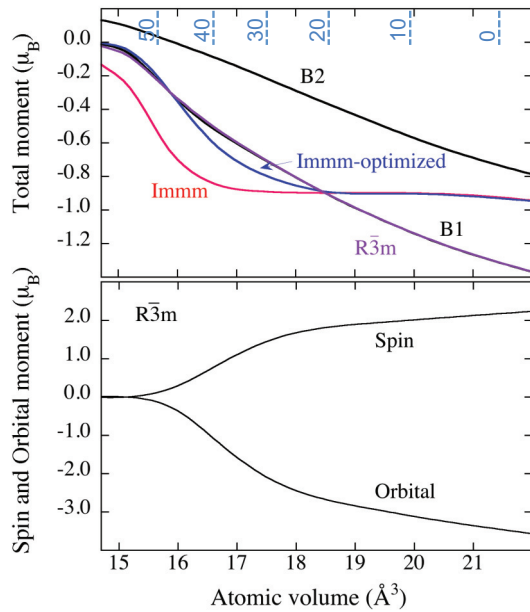
FIG. 5. (Color online) (a) Calculated total magnetic moments (spin and orbital contributions) for several candidate structures as functions of atomic volume. The lowest volume (14.7 Å^3) corresponds to about 65 GPa for the $R\bar{3}m$ (lowest energy) phase. Calculations imply that the B1 and $R\bar{3}m$ phases have nearly degenerate magnetic moments. (b) Spin and orbital components of the magnetic moment of the uranium atoms in the $R\bar{3}m$ phase versus atomic volume. The calculated pressures corresponding to the atomic volumes of the $R\bar{3}m$ phase are given across the top x axis in GPa.
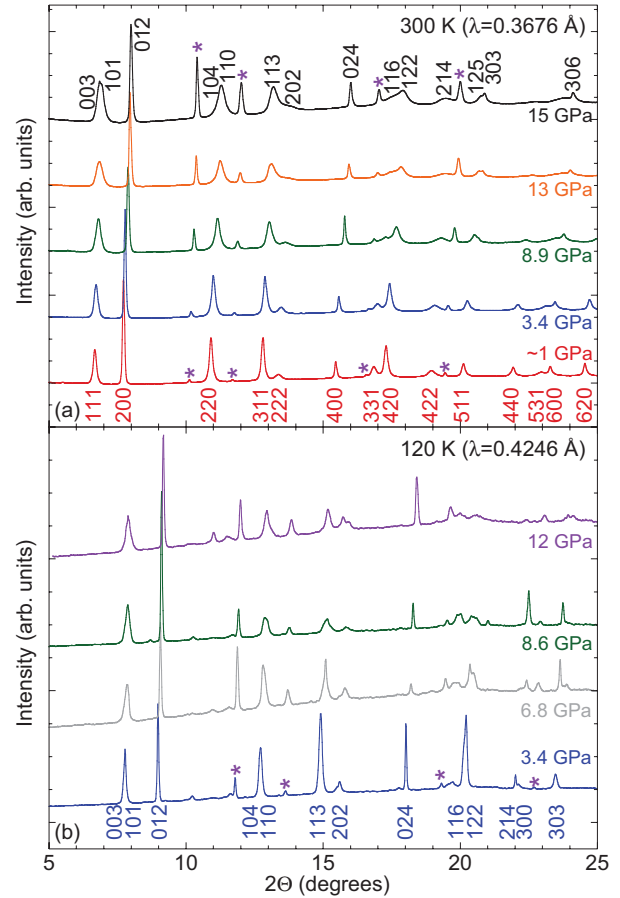

FIG. 6. (Color online) Diffraction patterns of US for selected pressures at 300 K (a) and 120 K (b). Patterns are offset vertically for clarity, the different incident wavelengths are noted, and the Cu pressure marker is denoted by a purple asterisk. For the 300-K data, the Bragg peaks for the B1 phase are labeled in red below the 1-GPa pattern, while those of the $R\bar{3}m$ phase are labeled (using hexagonal coordinates; see text) in black above the 15-GPa pattern. For the 120-K data, the Bragg peaks for the magnetically ordered $R\bar{3}m$ phase are labeled in blue below the 3.4-GPa pattern.

(s.g. $R\bar{3}m$, No. 166) that is a distortion of the B1 phase. At 120 K and ambient pressure, US is in an ordered ferromagnetic state, the onset of which results in rhombohedral distortion ($R\bar{3}m$) identical—albeit smaller in magnitude—to that seen under pressure. Applying pressure at 120 K compresses the rhombohedral lattice continuously. The rhombohedral unit cells at 300 and 120 K are indexed in Fig. 6 using hexagonal coordinates (see below).

Starting from 300 K and ambient pressure, increasing pressure or decreasing temperature into the ordered state results in a qualitatively identical distortion of the B1 phase. The rhombohedral unit cell breaks the fcc symmetry of the (111) planes of the B1 phase, resulting in a stretching of the lattice along one of the former body diagonal directions. This reduction in symmetry splits the B1 (111) Bragg peak, which has a multiplicity of eight, into two Bragg peaks in the $R\bar{3}m$ phase: the (003) peak with a multiplicity of two corresponding to the stretched body diagonal directions and the (101) peak with a multiplicity of six corresponding to the remaining body diagonals. Shown in Fig. 7, this distortion can be represented by one of three equivalent unit cells within the $R\bar{3}m$ space group: a hexagonal, a rhombohedral, or a pseudocubic (face-centered rhombohedral) basis.

The hexagonal unit cell [Fig. 7(a)] uses hexagonal coordinates for the $R\bar{3}m$ space group. It is defined by two lattice parameters a and c, and is composed of six atoms per cell with the U atoms residing at 3a (0,0,0) and the S atoms residing at 3b (0,0,$\frac{1}{2}$). The c axis of the hexagonal structure corresponds

to the stretched body diagonal [111] direction of the original B1 phase [Fig. 7(d)].

The rhombohedral unit cell [Fig. 7(b)] uses rhombohedral coordinates for the $R\bar{3}m$ space group. It can be constructed from the original B1 phase by setting each of the six face-centered U atoms and two diametrically opposed corner atoms as the vertices of the new unit cell, which contains two atoms per cell and is defined by a lattice parameter a and a cell angle α. In the B1 phase, this rhombohedral cell would have $\alpha = 60°$, but the high-pressure phase of US distorts to angles below 60°. In this rhombohedral cell, the U atoms reside at (0,0,0) and the S atoms reside at ($\frac{1}{2},\frac{1}{2},\frac{1}{2}$). The [111] direction of the rhombohedral cell corresponds to the [111] direction of the B1 phase that is stretched when the system undergoes its pressure-induced rhombohedral distortion [Fig. 7(e)].

Due to its clear relationship to the original B1 phase, the pseudocubic cell [Fig. 7(c)] is probably the most represented of these variants in the literature for US. Like the rhombohedral cell, the pseudocubic cell uses rhombohedral coordinates defined by a lattice parameter a and a cell angle α. Unlike
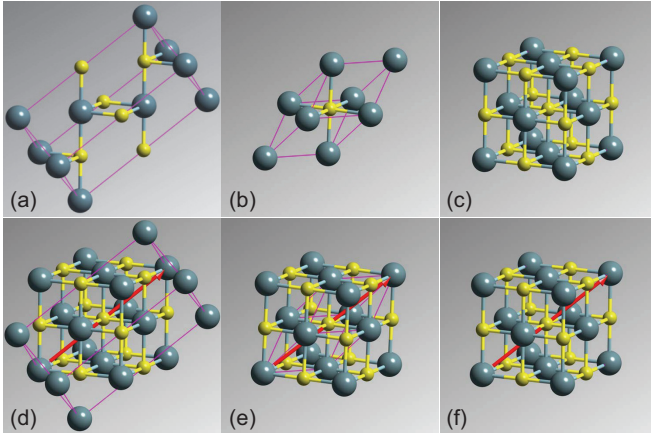
FIG. 7. (Color online) The three equivalent descriptions of the high-pressure rhombohedral phase of US. (a)–(c) Single unit cells in the hexagonal, rhombohedral, and pseudocubic (face-centered rhombohedral) bases, respectively. Green (larger) atoms are uranium, yellow (smaller) atoms are sulfur, U-S bonds are shown with both colors, and the solid, magenta line is the unit cell boundary [not seen in (c) or (f) due to bonds]. The equivalence of the structures is highlighted in (d)–(f), where the rocksalt-like bonding is extended outside the first unit cells of (a) and (b). The body diagonal that is expanded with respect to the ambient-pressure B1 structure is marked by the red arrow.

the rhombohedral cell, the pseudocubic cell would have $\alpha = 90°$ in the B1 phase, but, like the rhombohedral cell, the high-pressure phase does have a reduced cell angle. In the pseudocubic cell, which is a face-centered rhombohedral cell, the U atoms reside at $(0,0,0)$ and $(\frac{1}{2},\frac{1}{2},0)$ while the S atoms reside at $(\frac{1}{2},0,0)$ and $(\frac{1}{2},\frac{1}{2},\frac{1}{2})$, yielding a unit cell with eight atoms per cell, identical to B1. Like the rhombohedral cell, the pseudocubic [111] direction is the same as the stretched [111] direction of the B1 phase [Fig. 7(f)].

Figure 8(a) shows the atomic volume of US as a function of pressure P at 300, 120, and 55 K. At room temperature, the transition from the B1 phase to the rhombohedral phase near 11 GPa is not accompanied by a volume collapse. For the two lower temperature compression experiments, US is ferromagnetic and already rhombohedral at ambient pressure. There are no structural phase transition or unambiguous volume discontinuities under pressure at 120 or 55 K; however, the data do indicate the presence of a negative thermal expansion in the rhombohedral phase between 300 and 120 K. Negative thermal expansions have been associated with anomalous phonon stiffening or invar-like behavior,[52–54] but the mechanisms at work in the rhombohedral phase of US are unclear.

The data have been fitted with a third-order Birch-Murnaghan equation of state:[55]

$$P(V) = \frac{3}{2} B_0 \left[\left(\frac{V_0}{V}\right)^{(7/3)} - \left(\frac{V_0}{V}\right)^{(5/3)} \right]$$
$$\times \left\{ 1 + \frac{3}{4}(B_0' - 4) \left[\left(\frac{V_0}{V}\right)^{(2/3)} - 1 \right] \right\}, \quad (1)$$

where B_0 is the bulk modulus, V_0 is the ambient-pressure atomic volume, and B' is the first derivative of the bulk
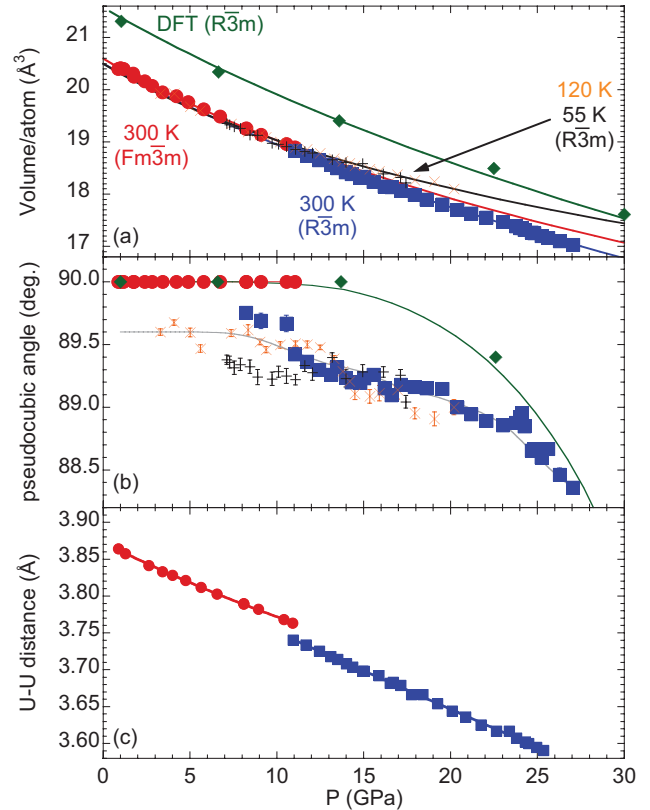

FIG. 8. (Color online) (a) Experimental equations of state for US under pressure in the B1 ($Fm\bar{3}m$; red circles) phase, as well as the $R\bar{3}m$ phase at room temperature (blue squares), 120 K (orange "x"), and 55 K (black "+"). The calculated equation of state (green diamonds) is also included for the $R\bar{3}m$ phase, which is the predicted zero-temperature ground state over this entire pressure range. The lines through the experimental data points as well as the calculations are fits to the third-order Birch-Murnaghan equation of state. (b) Experimental pseudocubic angle versus pressure in the B1 phase at room temperature and $R\bar{3}m$ phase at different temperatures as well as the predictions from DFT calculations. Error bars are derived from refinements. (c) Smallest U-U distance at room temperature in the B1 and $R\bar{3}m$ phases as a function of pressure. Lines in (b) and (c) are guides to the eye.

modulus. The parameters extracted from these fits are listed in Table II. The calculated equation of state [included in Fig. 8(a)] agrees well with the experimental data, with the exception of a 4% shift in the calculated volume.

The pseudocubic cell angle under pressure is shown in Fig. 8(b). In the B1 phase, the angle is, by definition, 90°. The cell angle of the rhombohedral phase decreases with increasing pressure, and the pressure dependence of that decrease is well captured by DFT calculations when considering only the sub-90° rhombohedral distortion. The region between about 8 and 11 GPa contains data points for both the B1 and $R\bar{3}m$ phases, because either of these phases can provide equal-quality descriptions of the diffraction data at those pressures. The cell angle does seem to show an abrupt departure from 90° in this region, yielding a change in the cell angle between 0.3° and 0.6° depending on what pressure is used to define the B1-$R\bar{3}m$ transition. Finally, the U-U nearest neighbor distance at 300 K is shown in Fig. 8(c). The rhombohedral distortion

TABLE II. Experimentally determined, best-fit parameters for the third-order Birch-Murnaghan equations of state [Eq. (1)] of US in the B1 phase at room temperature as well as the rhombohedral phase ($R\bar{3}m$) at room temperature and 55 K. Results from DFT calculations are included for comparison. V_0 is the atomic volume at ambient pressure, B_0 is the bulk modulus, and B' is the first derivative of the bulk modulus.

	V_0 (Å³)	B_0 (GPa)	B'
300 K ($Fm\bar{3}m$)	20.6	106.4	4.3
300 K ($R\bar{3}m$)	20.5	114.1	2.9
55 K ($R\bar{3}m$)	20.4	115.5	5.9
DFT ($R\bar{3}m$)	21.5	112.6	2.6

causes an abrupt change in the nearest neighbor distance, amounting to an approximately 0.6% reduction.

C. Electrical transport

The temperature dependence of the longitudinal electrical resistivity of US for various pressures is highlighted in Fig. 9. At the lowest measured pressure, 3.1 GPa, the electrical resistivity displays a positive curvature with increasing temperature; this curvature clearly gives way to a T-linear resistivity above about 190 K. At high temperatures, both magnetic and phonon scattering drive the temperature dependence of the electrical transport. However, below the Curie temperature, T_C, random spin-flip scattering is reduced, yielding the observed reduction of the electrical resistivity with decreasing temperature. The temperature-dependent electrical resistivity of a ferromagnet below T_C can be described by[56]

$$\rho(T) = \rho_0 + A_{\mathrm{mag}}T^2 + c_{ph}T, \qquad (2)$$

where ρ_0 is the residual resistivity, $\rho_{\mathrm{mag}} = A_{\mathrm{mag}}T^2$ parameterizes scattering from gapless magnetic excitations, and $\rho_{ph} = c_{ph}T$ characterizes the typical T-linear scattering expected from phonons for temperatures above the Debye temperature. The phonon contribution can be extracted from the
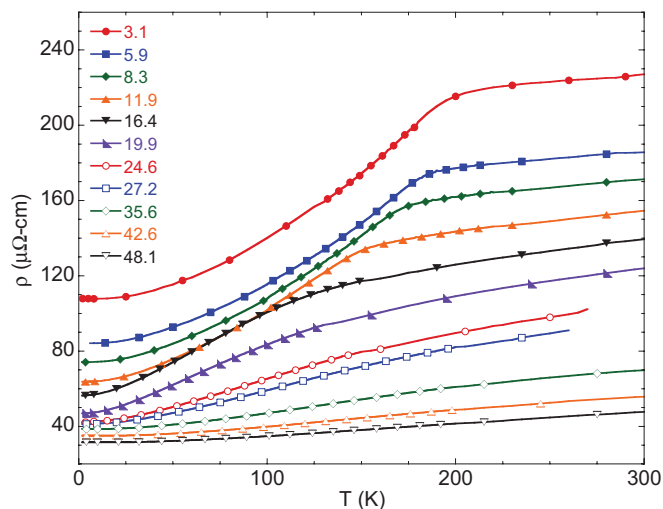

FIG. 9. (Color online) Electrical resistivity ρ as a function of temperature T for various pressures (denoted in the legend in GPa).
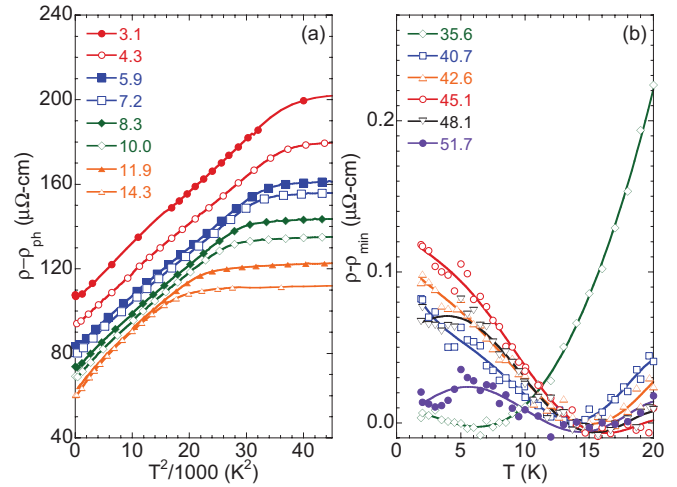

FIG. 10. (Color online) (a) Low-pressure magnetic and impurity scattering, $\rho - \rho_{ph}$, versus $T^2/1000$, highlighting the T^2 dependence of the resistivity in the ferromagnetic state. (b) Magnification of the high-pressure data, $\rho - \rho_{\mathrm{min}}$, showing the development of a negative slope at the lowest temperatures. Pressures are denoted in each legend in GPa.

high-temperature data ($T > T_C$) and subtracted from the electrical resistivity curves to yield the impurity and magnetic scattering contributions to the electrical resistivity. These contributions are plotted as $\rho - \rho_{ph}$ versus T^2 in Fig. 10(a), which clearly evinces the T^2 and T-linear behavior of the electrical resistivity below and above T_C, respectively.

With increasing pressure, both the 300- and 10-K values of the the electrical resistivity are suppressed (Fig. 9). The T-linear portion of the resistivity extends to lower temperatures, consistent with the suppression of the ferromagnetic state under pressure, but the low-temperature T^2 behavior remains, persisting to 14.3 GPa [Fig. 10(a)]. Above 14.3 GPa, the distinction between temperature regions described by T^2 or T-linear behavior becomes less clear. At the highest pressures ($P \gtrsim 35$ GPa), a negative slope in the electrical resistivity develops at low temperatures. This negative slope is displayed in Fig. 10(b), which plots the low-temperature resistivity difference—$\rho - \rho_{\mathrm{min}}$, where ρ_{min} is the value of the resistivity at the minimum temperature T_{min}—versus T.

Because the electrical resistivity is sensitive to changes in magnetic scattering, the $\rho(T)$ data can be used to track the pressure dependence of T_C. The temperature derivative of the resistivity $d\rho/dT$ is plotted as a function of T in Fig. 11(a). The sharp peak in $d\rho/dT$ seen at 3.1 GPa corresponds to T_C. The temperature dependence of $d\rho/dT$ shows a sharp transition up to 14.3 GPa, with the peak being suppressed to lower temperature with increasing pressure. This is consistent with the pressure range up to which Eq. (2) above holds. For $P \geqslant 16.4$ GPa, the shape of $d\rho/dT$ reveals a more gentle curvature leading to a broad maximum, which is denoted as T^*.

In addition to the longitudinal electrical resistivity, it has been shown that the transverse resistance in field (Hall resistance, R_{xy}) is also sensitive to the ferromagnetic transition in US.[56] The Hall resistance at 6 T is obtained by symmetrizing the data as $R_{xy} = R_{xy}(+6\,\mathrm{T}) - R_{xy}(-6\,\mathrm{T})/2$ and displayed in Fig. 11(b). The Hall resistance under pressure shows very
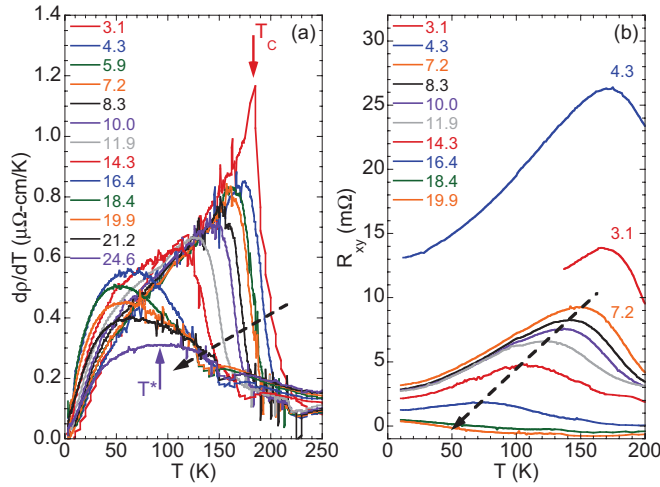
FIG. 11. (Color online) (a) Temperature derivative of the electrical resistivity versus temperature for pressures up to 24.6 GPa. The maximum associated with the steeper curvature is denoted as T_C ($P \leqslant 14.3$ GPa), while that associated with the gentler curvature is defined as T^* ($P \geqslant 16.4$ GPa). (b) Transverse magnetoresistance R_{xy} versus temperature for various pressures. The maximum in R_{xy} corresponds to the onset of ferromagnetism. Pressures are denoted in GPa, and the dashed arrows indicates the direction of increasing pressure.
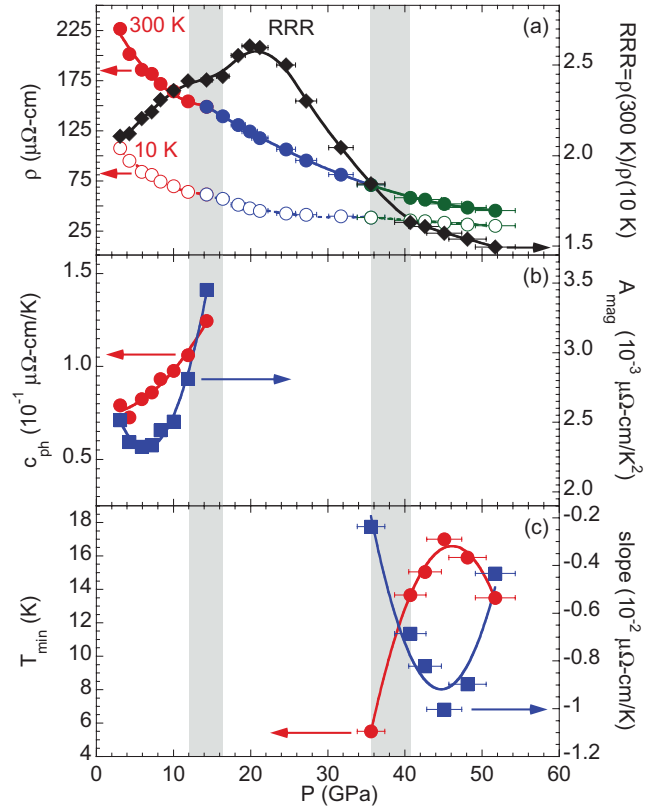

FIG. 12. (Color online) (a) The value of the electrical resistivity at 300 and 10 K as well as RRR versus pressure. (b) The pressure evolution of the coefficients for the phonon scattering (left axis) and magnetic scattering (right axis) terms describing the temperature dependence of the electrical resistivity at low pressure. (c) The pressure dependence of the minimum temperature T_{min} and the low-temperature slope for $T < T_{min}$. The gray shaded areas indicate pressure regions where RRR exhibits subtle changes in its pressure dependence. Arrows indicate the axis corresponding to each data set.

similar behavior to that of ambient-pressure measurements, displaying a maximum near T_C. This maximum is denoted here as T_H. For T near and below T_C, R_{xy} is dominated by the anomalous Hall effect, which is a consequence of the spontaneous magnetization induced by the onset of ferromagnetism.[57] Whether this anomalous Hall effect is driven by an intrinsic or extrinsic mechanism is unclear: The strong spin-orbit interaction of the uranium ions may suggest an increased propensity for an intrinsic origin, but similar behavior observed in heavy-fermion materials may argue for a genesis based in skew scattering.[58] With increasing pressure, the amplitude of the signature of R_{xy} is reduced and shifted to lower temperatures; for $P > 16.4$ GPa, there is no clear maximum, suggesting that the ferromagnetic state has been destroyed.

The quantities extracted from the electrical transport data are summarized in Fig. 12. The values of the electrical resistivity at 300 and 10 K are monotonically depressed with pressure [Fig. 12(a)]. In the range between 12–16 GPa, both $\rho(300$ K$)$ and $\rho(10$ K$)$ display kinks, and RRR = $\rho(300$ K$)/\rho(10$ K$)$ evinces a change in slope. In addition to the disappearance of the signature in R_{xy} that occurs in this pressure range, the T^2 behavior from Eq. (2) ceases [Fig. 12(b)]. Higher pressures reveals a maximum in RRR near 20 GPa followed by a decline. Near 38 GPa, another subtle change in slope is visible in RRR, and a slight kink can be discerned in $\rho(10$ K$)$. The minimum that develops in the electrical resistivity also manifests near 38 GPa. The pressure dependence of T_{min} and the slope of the electrical resistivity for $T < T_{min}$ are shown in Fig. 12(c). The electrical transport shows three regions of interest defined from Fig. 12: a low-pressure region below about 14 GPa where the room temperature phase is B1 and low-temperature scattering is

dominated by ferromagnetic scattering, an intermediate region where the room-temperature phase is $R\bar{3}m$ and the low-temperature scattering reveals a characteristic temperature T^*, and a high-pressure region above about 38 GPa where the room-temperature phase is unknown and the low-temperature scattering displays a minimum reminiscent of the Kondo effect. Whether this final high-pressure region is a consequence of a structural transition or a change in the electronic structure cannot be addressed with the current data.

The electronic and structural phase diagram induced from the electrical transport and structural characterizations above is shown in Fig. 13. Pressure drives T_C down, but, for $P > 14.3$ GPa, no evidence of ferromagnetic ordering is observed in the electrical transport data. The ferromagnetic state is thus bound to the low-pressure region shown by the blue, shaded region in Fig. 13. For pressures above about 18 GPa, the gentle maximum in $d\rho/dT$ defined as T^* is shown as the gray, shaded region in Fig. 13. Whether T^* simply represents a characteristic energy scale in the scattering mechanisms or whether it represents a thermodynamic phase boundary is not discernible from the electrical transport data. DFT calculations find that the ferromagnetic ground state is the only favorable magnetic phase. The pressure dependence
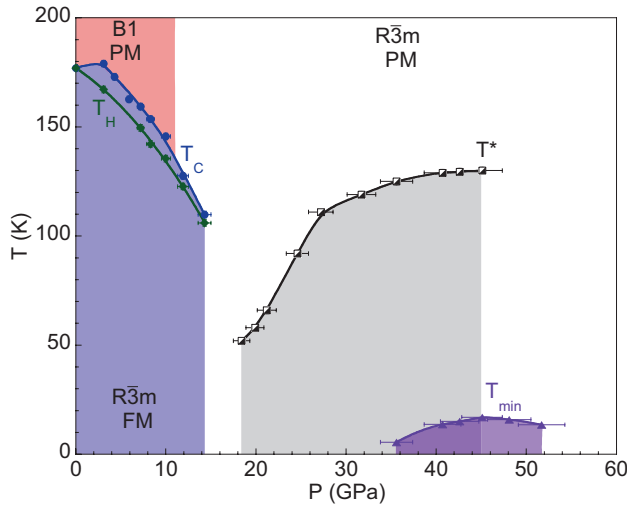
FIG. 13. (Color online) Temperature-pressure electronic and structural phase diagram of US. The paramagnetic portion (PM) of the phase diagram with cubic B1 symmetry is denoted by the red, shaded region, while the rhombohedral, ferromagnetic (FM) regime (blue, shaded region) is demarcated by T_C and T_H. For all pressures above approximately 11 GPa, experiment and theory suggest that the rhombohedral $R\bar{3}m$ structure is stable from 0–300 K. The gray and purple shaded regions highlight regimes of the phase diagram bounded by the characteristic temperatures T^* and T_{min}, respectively.

of T_{min} from Fig. 12(c) is included at the highest pressures, and the region of the phase space below T_{min}, where the slope of $\rho(T)$ is negative, is shown as the purple, shaded region.

IV. DISCUSSION

The destruction of magnetism with decreasing atomic volume is often discussed in the context of the Hill limit.[59] The Hill limit proposes a simple assertion that the separation between nearest neighbor U atoms is critical in determining the electronic ground state of the system by serving as a localization-delocalization boundary for the *5f* electrons. This boundary is generally regarded to be about 3.5 Å for U. In US, the U-U separation at ambient pressure is about 3.9 Å, for which the Hill limit concept would imply a ferromagnetic ground state. This is indeed true, although perhaps serendipitously. Previous experimental and theoretical results as well as our DFT calculations above indicate that US is better thought of as an itinerant rather than a localized *f*-electron system. While the ferromagnetic state is destroyed under pressure with lattice compression, the U-U nearest neighbor distance is only modestly affected, and remains above 3.7 Å for all pressures where ferromagnetic order is observed [Fig. 8(c)].

A more formal argument for the behavior of magnetic ordering in the U*X* system with pressure was put forth by Sheng *et al.*,[21] who propose that the pressure-induced loss of *f* occupancy and increase in hybridization are largely responsible for the observed behavior of T_C with pressure. Beginning from a localized system, this construct would suggest that pressure first drives T_C up due to an increasing exchange between local *f* moments, then, with increasing hybridization and loss of *f*-occupancy, pressure begins to

drive T_C down. This increasing and decreasing T_C is evidenced in UTe.[19] The calculations of Sheng *et al.* are in qualitative agreement with the pressure trends of each member of the U*X* system as well as the general chemical trends across the system. However, this model does not explain the abrupt disappearance of ferromagnetic order in the US, or the U*X* system in general.

An abrupt destruction of ferromagnetic order could be caused by a quenching of the U moments with pressure. However, according to our DFT calculations (Fig. 5) and consistent with those of Severin *et al.*,[22] pressure reduces the total moment only by about 15% by 14.3 GPa. While the reduction in moment with pressure may play a role in the reduction in T_C, it would seem insufficient to explain the abrupt disappearance of the ferromagnetic state.

The ferromagnetic-paramagnetic transition under pressure is at least sensitive to structural alterations. For USe, the abrupt loss of magnetic order is associated with a first-order structural phase transition from the B1 to B2 phase. For UTe, however, ferromagnetism persists into the B2 phase before abruptly disappearing. The B1-B2 transition alters the U-*X* coordination, changing the U ions from 6-fold to 8-fold coordinated, and this 8-fold U coordination presents an obvious impediment to the development of the rhombohedrally distorted ferromagnetic state observed in US and USe at ambient pressure. Given that in UTe, T_C persists despite a change in coordination and, in US, the structural phase transition (B1-$R\bar{3}m$) that destroys magnetic order does not generate a new coordination, it is difficult to implicate U-*X* coordination alone as a general driving force for the loss of ferromagnetic order in the U*X* system under pressure.

At ambient pressure, and with decreasing temperature, the B1 phase of US distorts to a rhombohedral structure to accommodate the ferromagnetic ground state. This distortion is temperature dependent, nearly scaling with the bulk magnetization of the ferromagnetic state and yielding a maximum distortion with a pseudocubic angle of 89.6°.[6] This means that there is a magnetostriction effect for the ferromagnetic state that pushes apart the (111) planes of the B1 phase. For low pressures in the ferromagnetic state, the pseudocubic angle of the $R\bar{3}m$ structure varies only slightly, going from about 89.6° at 4 GPa to 89.5° at 10 GPa [Fig. 8(b)]. Pressure thus drives the rhombohedral distortion of the B1 phase in the same direction [i.e., pushing apart the original B1 (111) planes] as the onset of ferromagnetic order at ambient pressure. It is somewhat counterintuitive then that increasing the magnitude of this distortion is unfavorable to ferromagnetic order. For $P > 10$ GPa, the pressure dependence of the pseudocubic angle steepens, decreasing to approximately 89.0° by 20 GPa. The magnitude of the pseudocubic angle may be critical to the ferromagnetic ground state, although the underlying physical mechanism that correlates magnetic order with the pseudocubic angle is not obvious, or it may be completely uncorrelated with magnetic order. It is unfortunately difficult to make a firm conclusion on this matter.

Finally, the loss of ferromagnetic order in US may be driven by a change in magnetic exchange, and thus a change in the type of magnetic order. It is possible that the high-pressure region of the electronic phase diagram—shown

as a gray region demarcated by black, hatched squares in Fig. 13—harbors another magnetically ordered state that is not ferromagnetic. Such a possibility is tantalizing in that it might provide a unifying description of the high-pressure behavior of magnetism in the U*X* system. The possibility of other magnetic ordering under pressure is encouraged by the appearance of resistive anomalies in the B2 phase of UTe.[19] If these hypothetical, high-pressure magnetic states possess only a small ordered moment (e.g., antiferromagnetism), then the ac susceptibility measurements of Cornelius *et al.*[20] may have been insensitive to their presence. However, the lack of any resistive signatures in the B2 phase of USe[60] and our own theoretical calculations that suggest that the ferromagnetic ground state is the lowest energy do not favor the appearance of additional magnetically ordered states. Confirming the speculation of other high-pressure, magnetically ordered states in US, USe, or UTe will require the development of more complicated theoretical models combined with other additional experimental high-pressure probes (e.g., resonant x-ray diffraction, neutron diffraction, x-ray magnetic dichroism, etc.) that could be sensitive to magnetic order other than ferromagnetism. Furthermore, high-pressure dichroic measurements of the nominally nonmagnetic chalcogen atoms (e.g., at the Se K edge) of the U*X* system may provide valuable information about the magnetism under pressure.[61,62]

V. CONCLUSIONS

We have measured the electronic and structural phase diagram of US to high pressures using electrical transport and x-ray diffraction. Ferromagnetic order is suppressed with pressure, abruptly disappearing near a pressure-induced rhombohedral ($R\bar{3}m$) distortion. This pressure-induced distortion is qualitatively identical to but stronger in magnitude than the distortion that occurs upon entering the ferromagnetic state at ambient pressure. The structural distortion is well captured by DFT calculations, which imply that the structural stability of the $R\bar{3}m$ phase is driven by its lower band energy. As DFT calculations predict a nonzero U moment up to high compressions, the destruction of magnetic order with the appearance of the $R\bar{3}m$ phase remains a mystery, but simple arguments based on the Hill limit or changes in structural coordination can most likely be ruled out. At higher pressures, the electrical transport measurements reveal new phase regions that may be important to understanding the magnetostructural free energy landscape of US.

[1] P. Santini, R. Lemanski, and P. Erdos, Adv. Phys. **48**, 537 (1999).

[2] F. A. Wedgwood, J. Phys. C: Solid State Phys. **5**, 2427 (1972).

[3] W. J. L. Buyers, T. M. Holden, J. A. Jackman, A. F. Murray, P. de V. DuPlessis, and O. Vogt, J. Magn. Magn. Mater. **31–34**, 229 (1983).

[4] G. H. Lander, M. S. S. Brooks, B. Lebech, P. J. Brown, O. Vogt, and K. Mattenberg, Appl. Phys. Lett. **57**, 989 (1990).

[5] J. A. C. Marples, J. Phys. Chem. Solids **31**, 2431 (1970).

[6] T. Herrmannsdörfer, P. Fischer, K. Mattenberger, and O. Vogt, J. Alloys Compd. **414**, 14 (2006).

[7] M. Erbudak and F. Meier, Physica B + C **102**, 134 (1980).

[8] S. P. Collins, D. Laundy, C. C. Tang, and G. van der Laan, J. Phys.: Condens. Matter **7**, 9325 (1995).

[9] N. Kernavanois, P. Dalmas de Réotier, A. Yaouanc, J.-P. Sanchez, V. Honkimäki, T. Tschentscher, J. McCarthy, and O. Vogt, J. Phys.: Condens. Matter **13**, 9677 (2001).

[10] T. Okane, J. Okamoto, K. Mamiya, S.-I. Fujimori, Y. Saitoh, U. Muramatsu, A. Fujimori, and A. Ochiai, Physica B **345**, 221 (2004).

[11] J. R. Jeffries, K. T. Moore, N. P. Butch, and M. B. Maple, Phys. Rev. B **82**, 033103 (2010).

[12] J. Grunzweig-Genossar, M. Kuznietz, and F. Friedman, Phys. Rev. **173**, 562 (1968).

[13] M. Erbudak and J. Keller, Z. Physik. B **32**, 281 (1979).

[14] J. M. Fournier and R. Troc, in *Handbook on the Physics and Chemistry of the Actinides*, edited by A. J. Freeman and G. H. Lander (North-Holland, Amsterdam, 1984), Vol. 2, p. 29.

[15] J. Schoenes, in *Handbook on the Physics and Chemistry of the Actinides*, edited by A. J. Freeman and G. H. Lander (North-Holland, Amsterdam, 1984), Vol. 2, p. 341.

[16] J. Schoenes and P. Brüesch, Solid State Commun. **38**, 151 (1981).

[17] J. A. Jackman, T. M. Holden, W. J. L. Buyers, P. de V. DuPlessis, O. Vogt, and J. Genossar, Phys. Rev. B **33**, 7144 (1986).

[18] L. Gerward, J. Staun-Olsen, U. Benedict, S. Dabos, and O. Vogt, High Press. Res. **1**, 235 (1989).

[19] P. Link, U. Benedict, J. Wittig, and H. Wühl, J. Phys.: Condens. Matter **4**, 5585 (1992).

[20] A. L. Cornelius, J. S. Schilling, O. Vogt, K. Mettenberger, and U. Benedict, J. Magn. Magn. Mater. **161**, 169 (1996).

[21] Q. G. Sheng and B. R. Cooper, J. Magn. Magn. Mater. **164**, 335 (1996).

[22]L. Severin, M. S. S. Brooks, B. Johansson, and J. Kübler, J. Magn. Magn. Mater. **140–144**, 1423 (1995).

[23]G. H. Lander, M. H. Mueller, D. M. Sparlin, and O. Vogt, Phys. Rev. B **14**, 5035 (1976).

[24]S. T. Weir, J. Akella, C. Aracne-Ruddle, Y. Vohra, and S. A. Catledge, Appl. Phys. Lett. **77**, 3400 (2000).

[25]J. R. Patterson, S. A. Catledge, Y. K. Vohra, J. Akella, and S. T. Weir, Phys. Rev. Lett. **85**, 5364 (2000).

[26]D. D. Jackson, J. R. Jeffries, W. Qiu, J. D. Griffith, S. McCall, C. Aracne, M. Fluss, M. B. Maple, S. T. Weir, and Y. K. Vohra, Phys. Rev. B **74**, 174401 (2006).

[27]H. K. Mao, J. Xu, and P. M. Bell, J. Geophys. Res. **91**, 4673 (1986).

[28]W. L. Vos and J. A. Schouten, J. Appl. Phys. **69**, 6744 (1991).

[29]A. Hammersley, S. Svensson, M. Hanfland, A. Fitch, and D. Häusermann, High Press. Res. **14**, 235 (1996).

[30]P. Söderlind, O. Eriksson, B. Johansson, and J. M. Wills, Phys. Rev. B **50**, 7291 (1994).

[31]P. Söderlind and A. Gonis, Phys. Rev. B **82**, 033102 (2010).

[32]R. Ahuja, P. Söderlind, J. Trygg, J. Melsen, J. M. Wills, B. Johansson, and O. Eriksson, Phys. Rev. B **50**, 14690 (1994).

[33]P. Söderlind, Adv. Phys. **47**, 959 (1998).

[34]J. P. Perdew, J. A. Chevary, S. H. Vosko, K. A. Jackson, M. R. Pederson, D. J. Singh, and C. Fiolhais, Phys. Rev. B **46**, 6671 (1992).

[35]J. M. Wills, O. Eriksson, M. Alouani, and D. L. Price, in *Electronic Structure and Physical Properties of Solids*, edited by H. Dreysse (Springer-Verlag, Berlin, 1998), p. 148.

[36]J. Trygg, J. M. Wills, M. S. S. Brooks, B. Johansson, and O. Eriksson, Phys. Rev. B **52**, 2496 (1995).

[37]P. Söderlind, Europhys. Lett. **55**, 525 (2001).

[38]P. Söderlind, A. Landa, and B. Sadigh, Phys. Rev. B **66**, 205109 (2002).

[39]P. Söderlind and B. Sadigh, Phys. Rev. Lett. **92**, 185702 (2004).

[40]O. K. Andersen, Phys. Rev. B **12**, 3060 (1975).

[41]L. Nordström, J. M. Wills, P. H. Andersson, P. Söderlind, and O. Eriksson, Phys. Rev. B **63**, 035103 (2000).

[42]K. T. Moore, G. van der Laan, R. G. Haire, M. A. Wall, A. J. Schwartz, and P. Söderlind, Phys. Rev. Lett. **98**, 236402 (2007).

[43]P. Söderlind, Phys. Rev. B **77**, 085101 (2008).

[44]O. Eriksson, M. S. S. Brooks, and B. Johansson, Phys. Rev. B **41**, 9087 (1990).

[45]L. Severin, M. S. S. Brooks, and B. Johansson, Phys. Rev. Lett. **71**, 3214 (1993).

[46]L. Vitos, *Computational Quantum Mechanics for Materials Engineers: The EMTO Method and Applications* (Springer, London, 2007).

[47]L. V. Pourovskii, A. V. Ruban, L. Vitos, H. Ebert, B. Johansson, and I. A. Abrikosov, Phys. Rev. B **71**, 094415 (2005).

[48]Kollar, L. Vitos, and H. L. Skriver, in *Electronic Structure and Physical Properties of Solids: The Uses of the LMTO Method*, Lecture Notes in Physics, edited by H. Dreyss (Springer, Berlin, 2000), pp. 85-113.

[49]A. Landa and P. Söderlind, J. Alloys Compd. **354**, 99 (2003).

[50]T. Shishidou and T. Oguchi, Phys. Rev. B **62**, 11747 (2000).

[51]T. Le Bihan, A. Bombardi, M. Iridi, S. Heathman, and A. Lindbaum, J. Phys.: Condens. Matter **14**, 10595 (2002).

[52]B. Fultz, Prog. Mater. Sci. **55**, 247 (2010).

[53]R. J. Weiss, Proc. Phys. Soc. **62**, 28 (1963).

[54]A. C. Lawson, J. A. Roberts, B. Martinez, M. Ramos, G. Kotliar, F. W. Trouw, M. R. Fitzsimmons, M. P. Hehlen, J. C. Lashley, H. Ledbetter, R. J. McQueeney, and A. Migliori, Philos. Mag. B **86**, 2713 (2006).

[55]F. Birch, Phys. Rev. **71**, 809 (1947).

[56]J. Schoenes, B. Frick, and O. Vogt, Phys. Rev. B **30**, 6578 (1984).

[57]N. Nagaosa, J. Sinova, S. Onoda, A. H. MacDonald, and N. P. Ong, Rev. Mod. Phys. **82**, 1539 (2010).

[58]Y. B. Ning, J. D. Garrett, C. V. Stager, and W. R. Datars, Phys. Rev. B **46**, 8201 (1992).

[59]H. H. Hill, in *Plutonium 1970 and Other Actinides*, edited by W. N. Miner (The Metallurgical Society of the AIME, New York, 1970).

[60]P. Link, U. Benedict, J. Wittig, and H. Wühl, Physica B **190**, 68 (1993).

[61]D. Mannix, A. Stunault, N. Bernhoeft, L. Paolasini, G. H. Lander, C. Vettier, F. de Bergevin, D. Kaczorowski, and A. Czopnik, Phys. Rev. Lett. **86**, 4128 (2001).

[62]M. Usuda, J.-I. Igarashi, and A. Kodama, Phys. Rev. B **69**, 224402 (2004).